

# Evolution of laser-fired aluminum-silicon contact geometry in photovoltaic devices

A. Raghavan,<sup>1</sup> T. A. Palmer,<sup>2</sup> and T. DebRoy<sup>1,a)</sup>

<sup>1</sup>*Department of Materials Science and Engineering, The Pennsylvania State University, University Park, Pennsylvania 16802-5005, USA*

<sup>2</sup>*Applied Research Laboratory, The Pennsylvania State University, USA*

(Received 11 November 2011; accepted 13 December 2011; published online 17 January 2012)

The evolution of temperature and velocity fields during laser processing of solar cells to produce an ohmic contact between an aluminum thin film and a silicon wafer is studied using a transient numerical heat transfer and liquid metal flow model. Since small changes in pulse duration, power, and power density can result in significant damage to the substrate and, in extreme cases, expulsion of droplets from the molten zone, the selection of optimal laser processing parameters is critical. The model considers the unusually large heat of fusion of the Al-Si alloy formed during processing and the large composition-dependent two phase region. The calculated size and shape of the fusion zone were in good agreement with the corresponding experimental data, indicating the validity of the model and providing a basis for using the model to develop a better understanding of the laser-assisted fabrication of contacts for solar cell devices. The transient changes in the composition of the Al-Si molten region are found to have a major impact on the heat transfer during the formation of the contact. Consideration of the time-dependent concentration of Al in the molten region is also essential to achieve good agreement between the experimental and computed molten pool sizes. Process maps showing peak temperatures and the depth and width of the molten pool are presented in order to assist users in the selection of safe process parameters for the rapid fabrication of these silicon-based photovoltaic devices. © 2012 American Institute of Physics. [doi:10.1063/1.3675442]

## INTRODUCTION

Lasers offer an attractive option for improving the processing efficiency of photovoltaic (PV) solar cell devices, particularly those utilizing a passivated emitter and rear cell (PERC) structure.<sup>1–8</sup> In the PERC structure, the backside of the Si wafer is covered by a thin-film metallic contact layer, such as Al, placed over thin SiO<sub>2</sub> and hydrogenated amorphous Si ( $\alpha$ -Si:H) passivation layers. Figure 1(a) shows a schematic diagram of the structure considered here. An ohmic contact must be formed between this thin film metallic layer and the underlying Si wafer for the cell to operate efficiently. Traditionally, these ohmic contacts are formed using a combination of photolithography, chemical etching, and high-temperature annealing.<sup>3,4</sup> In addition to being expensive and time-consuming, thermal stresses induced from high temperature annealing can cause warpage and fracture of the Si wafer. On the other hand, laser processing of these contacts offers a cost-effective alternative that can streamline the overall production process, reduce energy usage and cost, and eliminate additional handling steps.

A laser-fired ohmic contact can be defined as a micro-joint between the Al thin film layer and the Si substrate. Laser processing using pulse durations ranging from milliseconds to nanoseconds with a range of different laser wavelengths is characterized by rapid melting and solidification,<sup>9</sup>

alloying element vaporization,<sup>10,11</sup> and droplet ejection.<sup>12</sup> These processes can take place simultaneously over several microseconds with extremely rapid heating and cooling rates on the order of thousands of degrees per second. Power levels from tens to thousands of watts and spot sizes on the order of tens of microns are used to generate these ohmic contacts.<sup>13,14</sup> With such a wide range of processing parameters available, it is important to understand how small changes in laser processing parameters affect the thermal cycles experienced by the substrate material. When these conditions are not adequately controlled, thermally induced damage can result in the contact and heat-affected zone (HAZ).<sup>15,16</sup> Furthermore, as processing parameters are varied, the size of the molten pool will change, playing a considerable role in attaining optimal device performance.<sup>1,17</sup>

Mathematical models can be used to predict and evaluate the temperature profiles and molten pool shape and size during arc and laser spot welding.<sup>18–25</sup> These models simultaneously solve equations of conservation of mass, momentum, and energy in calculating the temperatures and liquid flow velocities in the molten zone and surrounding areas. Since the laser process used to generate these contacts approximates that for laser spot micro-welding, similar methodologies can be developed to model laser-fired contact (LFC) formation and to understand the mechanisms that drive the melting phenomenon observed in binary Al-Si alloys as a function of laser processing parameters.

Here, we examine the impact of variations in pulse duration and power levels on the molten pool geometry, thermal

<sup>a)</sup>Author to whom correspondence should be addressed. Electronic mail: rtd1@psu.edu.

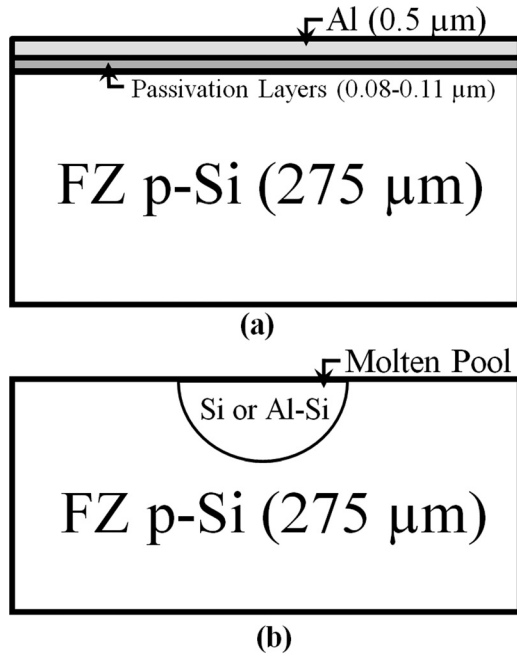


FIG. 1. Schematic diagram of (a) experimental substrate and (b) modeled substrate that uses Si material properties in bulk substrate and Si or Al-Si properties within molten region.

cycles, and fluid velocities during the laser processing of a 275- $\mu\text{m}$ -thick Si substrate coated with a 0.5- $\mu\text{m}$ -thick Al thin film. The impact of compositional changes due to the dissolution of the Al thin film in the molten region is addressed. Since the temperature difference between the liquidus and eutectic temperatures for the Al-Si material system can reach 800 K at certain alloy compositions, a method was developed to calculate the liquid fraction present in the two-phase region. By taking into account the Al content in the molten region, the correlation between experimental results and theoretical calculations for the measured molten pool diameter at various power levels and pulse durations is significantly improved. The computed size of the molten pool is compared with that obtained from modeling for various laser processing conditions. Process maps showing how the peak temperature and the depth and width of the molten pool

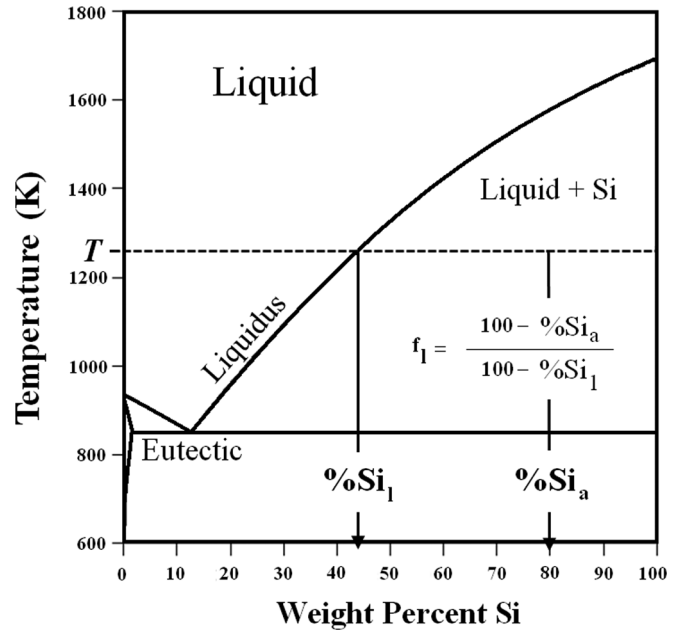


FIG. 3. Al-Si binary phase diagram.

change with laser processing parameters are then produced using this computational model.

## EXPERIMENTS AND MODEL DEVELOPMENT

Silicon wafers with a thickness of 275  $\mu\text{m}$  were coated with a 0.5- $\mu\text{m}$ -thick Al contact layer deposited via an electron beam physical vapor deposition process.<sup>13</sup> A schematic diagram of the sample structure used in the model is shown in Fig. 1(b). The presence of the passivated layer shown in Fig. 1(a) is not considered because of its small thickness. An IPG Photonics® 1070 nm single mode fiber laser with an experimentally determined beam size of 20  $\mu\text{m}$  at focus was used. The laser powers studied were 18 W, 34 W, and 50 W with pulse durations of 4 ms, 9 ms, 14 ms, and 19 ms. Model validation is performed using experimental measurements for the top surface of the laser-fired spots.

A well-tested,<sup>9-12</sup> three-dimensional numerical model was used to calculate the temperature profiles and molten pool geometry of the laser spots. Since the details of the computational model are available elsewhere,<sup>12,19</sup> only a brief description of the model, emphasizing the addition of new features, is presented. Non-uniform grid spacing, typically  $135 \times 70 \times 55$  grids and 50 microsecond time steps were used to maintain computational accuracy. The solution domain had dimensions in the x, y, and z directions of 800  $\mu\text{m}$ , 400  $\mu\text{m}$ , and 275  $\mu\text{m}$ , respectively. Finer grid spacing was used in the area below the laser beam to achieve maximum resolution of variables, and the minimum grid spacing was approximately 1  $\mu\text{m}$  in the x, y, and z directions.

The model uses a finite difference-based control volume method<sup>26</sup> to calculate the fluid flow velocities and temperatures by solving the equations for the conservation of mass (1), momentum (2), and energy (3) in a Cartesian coordinate system,

### Top Surface:

$$\mu \frac{\partial u}{\partial z} = f_L \frac{dy}{dT} \frac{dT}{dx}$$

$$\mu \frac{\partial v}{\partial z} = f_L \frac{dy}{dT} \frac{dT}{dy}$$

$$w = 0 \text{ cm/sec}$$

### Other Surfaces:

$$T = 298 \text{ K}$$

$$u = v = w = 0 \text{ cm/sec}$$

### Symmetry Surface:

$$\frac{\partial u}{\partial y} = 0 \quad \frac{\partial w}{\partial y} = 0$$

$$v = 0 \text{ cm/sec}$$

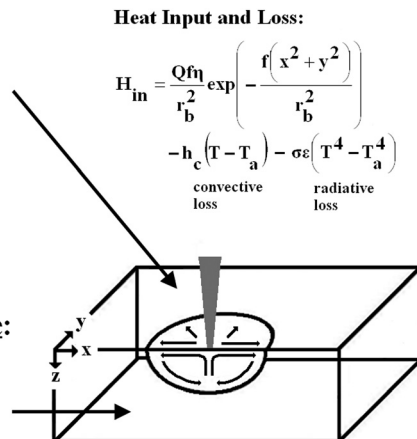


FIG. 2. Boundary conditions applied to solve conservation equations.

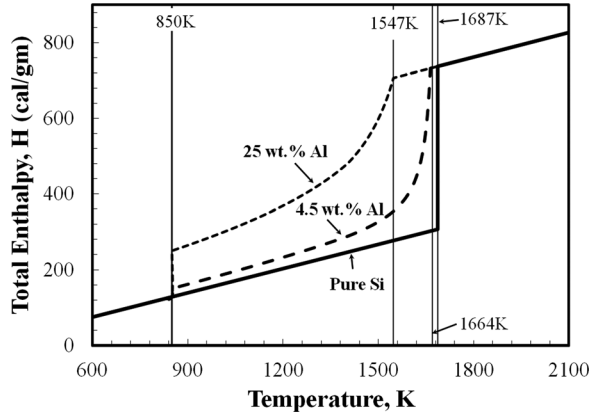


FIG. 4. Plot of enthalpy as a function of temperature that shows the amount of energy that is required for melting in the two-phase region for alloys with additions of Al (25 wt. % and 4.5 wt. %).

$$\frac{\partial(\rho u_i)}{\partial x_i} = 0, \quad (1)$$

where,  $\rho$  is the density,  $x_i$  is the distance along the  $i = 1, 2$ , and 3 directions, and  $u_i$  is the velocity component along the  $i$  direction.

$$\frac{\partial(\rho u_j)}{\partial t} + \frac{\partial(\rho u_j u_i)}{\partial x_i} = \frac{\partial}{\partial x_i} \left( \mu \frac{\partial u_j}{\partial x_i} \right) + S_j, \quad (2)$$

where  $t$  is the time,  $u_j$  is the velocity component along the  $j$  direction,  $\mu$  is the effective viscosity, and  $S_j$  is a source term for the  $j$  component momentum equation.

TABLE I. Data used for calculations.

Property	Value	Reference
Density of liquid Si ( $\text{kg m}^{-3}$ )	2510	27
Density of liquid Al ( $\text{kg m}^{-3}$ )	2390	27
Absorptivity of solid Al	0.1–0.4	28
Absorptivity of liquid Si	0.223	29
Effective viscosity ( $\text{kg m}^{-1} \text{s}^{-1}$ )	0.0088	30–32
Melting temperature (K), pure Si	1687	33
Solidus temperature (K), Al–Si alloy	850	33
Liquidus temperature (K), Al–Si alloy	1551–1664	33
Enthalpy of solid at melting point ( $\text{kJ kg}^{-1}$ ), pure Si	1286	34
Enthalpy of solid at solidus ( $\text{kJ kg}^{-1}$ ), Al–Si alloy <sup>a</sup>	536	...
Enthalpy of liquid at melting point ( $\text{kJ kg}^{-1}$ ), pure Si	3085	34
Enthalpy of liquid at liquidus ( $\text{kJ kg}^{-1}$ ), Al–Si alloy <sup>a</sup>	2961–3064	...
Specific heat of solid ( $\text{kJ kg}^{-1} \text{K}^{-1}$ )	0.895	34
Specific heat of liquid ( $\text{kJ kg}^{-1} \text{K}^{-1}$ )	0.908	34
Specific heat of two-phase region ( $\text{kJ kg}^{-1} \text{K}^{-1}$ ) <sup>a</sup>	0.895	...
Thermal conductivity of solid ( $\text{J m}^{-1} \text{s}^{-1} \text{K}^{-1}$ )	36	35
Effective thermal conductivity of liquid ( $\text{J m}^{-1} \text{s}^{-1} \text{K}^{-1}$ )	218	35–37
Thermal coefficient of surface tension ( $\text{mN m}^{-1} \text{K}^{-1}$ )	–0.13	27, 38
Coefficient of thermal expansion	2.3 E–06	37

<sup>a</sup>Values extrapolated from data in Figs. 3 and 4.

$$\rho \frac{\partial(h)}{\partial t} + \frac{\partial(\rho u_i h)}{\partial x_i} = \frac{\partial}{\partial x_i} \left( \frac{k}{C_p} \frac{\partial h}{\partial x_i} \right) - \rho \frac{\partial(\Delta H)}{\partial t} - \rho \frac{\partial(u_i \Delta H)}{\partial x_i}, \quad (3)$$

where  $C_p$  is the specific heat,  $h$  is the sensible heat, and  $\Delta H$  is the latent heat content. The equations were discretized for each variable by integrating over the control volumes in the computational domain and iteratively solved on a line-by-line basis using the tri-diagonal matrix algorithm<sup>26</sup> to determine the value of the dependent variables.

Figure 2 shows a schematic diagram of the boundary conditions used in the solution of these equations. Since the laser-fired contact is symmetric about the centerline, only half the work piece was considered, and the weld top surface is assumed to be flat. The power density distribution of the laser on the top surface was determined using the following relationship:

$$H_{in} = \frac{qf\eta}{r_b^2} \exp\left(-\frac{f(x^2 + y^2)}{r_b^2}\right), \quad (4)$$

where  $f$  is the heat distribution factor,  $q$  is the laser power,  $\eta$  is the absorptivity of the laser energy at the work piece,  $r_b$  is the laser beam radius, and  $x$  and  $y$  represent the coordinates used to calculate the power distribution at that particular location. The distribution factor is given a value of 3.0 to replicate the Gaussian beam power density distribution output from the fiber laser.<sup>20</sup>

The Al–Si phase diagram, which is shown in Fig. 3, was used to determine the liquidus temperature and liquid fraction at various compositions and temperatures. As the molten pool size changes with variations in laser processing parameters, the concentration of Al in solution will change, since the thickness of the Al thin film is constant and no Al is added to the system. With changes in Al concentration, the difference between the liquidus and solidus temperatures will also change based on the phase diagram. Depending on the concentration of Al in the binary alloy, the difference between the eutectic and liquidus temperatures can be greater than 800 K. Therefore, an accurate determination of the amount of energy needed to raise the temperature of the material or melt an incremental fraction of solid in the two-phase region is critical to calculate the thermal cycles and spot size accurately.

Depending on the alloy composition, the total enthalpy in the system,  $H$ , can vary widely over the two-phase (liquid + Si) region. The relationship between the sensible heat,  $h$ , latent heat content,  $\Delta H$ , and total enthalpy is defined as

$$H = h + \Delta H. \quad (5)$$

The sensible heat,  $h$ , is calculated as

$$h = \int C_p dT, \quad (6)$$

where  $C_p$  is the specific heat and  $T$  is the temperature. The latent heat content,  $\Delta H$ , is calculated as

$$\Delta H = f_L \times L, \quad (7)$$

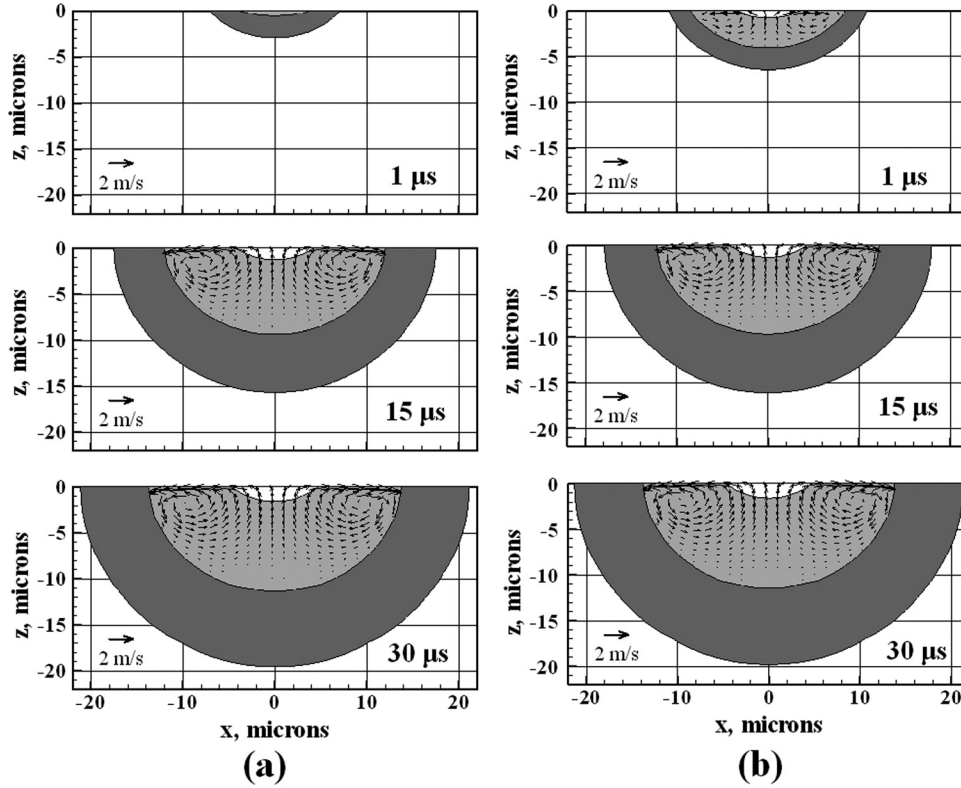


FIG. 5. Calculated molten pool cross sections for 25-W laser power and 20- $\mu\text{m}$  spot diameter for absorptivity values of (a) 0.1, then 0.223 for temperatures greater than 933 K and (b) 0.4, then 0.223 for temperatures greater than 933 K.

where  $L$  is an approximated latent heat of fusion for pure Si or an Al-Si alloy. To accurately determine the amount of liquid present at any given temperature, the lever rule for binary phase diagrams is used. The fraction of liquid present at each temperature is determined using the following relationship:

$$f_L = \frac{100 - \%Si_a}{100 - \%Si_l}, \quad (8)$$

where  $f_L$  is the liquid fraction,  $\%Si_a$  is the concentration of Si in the alloy, and  $\%Si_l$  is the concentration of Si in the liquid at temperature  $T$ . It is necessary to use an approximation of the relationship between composition and temperature for the liquidus line on the Al-Si phase diagram to calculate this value. These functions, shown below, were obtained by fitting two curves to the liquidus line on the Al-Si phase diagram shown in Fig. 3.

$$\%Si_l = \begin{cases} (T/145.62 - 2.25)^2 - 0.345279 & \text{for } T_{\text{solid}} \leq T < 1404 \\ 1.73 \times 10^{-9} T^{3.335} & \text{for } 1404 \leq T \leq T_{\text{liquid}} \end{cases} \quad (9)$$

Equation (9) is used to determine the concentration of Si in the liquid at any given temperature over the two-phase region. Using Eqs. (8) and (9), the liquid fraction can be approximated for an alloy with a given concentration of Si. The concentration of Si is determined by first approximating the concentration of Al in the molten pool based on the Al layer thickness. The concentration of Al in the Al-Si molten region was calculated assuming that the Al directly above the molten region dissolves into the molten pool. The concentration of Al in solution was calculated as

$$wt.\%Al = \frac{V_{Al}\rho_{Al}}{V_{Si}\rho_{Si} + V_{Al}\rho_{Al}} \times 100, \quad (10)$$

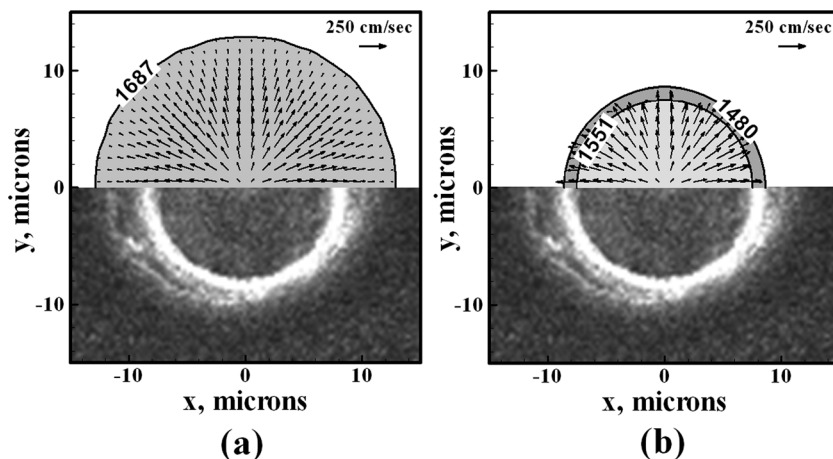


FIG. 6. Comparison between the experimental (Ref. 13) and computed sizes of the molten region when modeling laser melting of (a) pure Si and (b) Al-Si alloy for a laser power of 18 W and pulse duration of 19 ms.



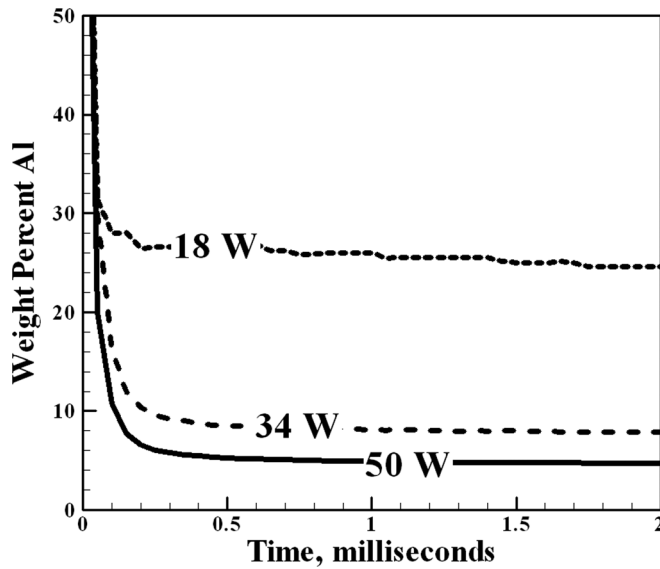


FIG. 7. Concentration of Al in molten pool approaches constant value within 0.2 ms for all laser powers.

where  $V_{Si}$  and  $V_{Al}$  are the volumes of Si and Al in the molten region, respectively, and  $\rho_{Si}$  and  $\rho_{Al}$  are the densities of liquid Si and liquid Al, respectively.

The concentration of Si in the molten pool,  $\%Si_a$ , which is used in Eq. (8) to calculate the liquid fraction in the model for each power level as a function of temperature is the balance of these values, since the system under consideration is an Al-Si binary alloy. After calculating the liquid fraction based on Eq. (8), the latent heat content can be calculated over the two-phase region per Eq. (7). The latent heat content is used in Eq. (5) to determine the total enthalpy for any given alloy system, and a comparison of the total enthalpy for three systems is shown in Figure 4. This figure shows the total enthalpy versus temperature for alloys with 25 wt. % Al and 4.5 wt. % Al and pure Si. The area under the curve represents the total energy required for melting, and the differences between the alloy systems versus the pure material will affect the melting behavior. Table I shows the material properties used for both pure Si and the binary Al-Si alloy.<sup>27–38</sup>

## RESULTS AND DISCUSSION

At the onset of laser processing, there is an Al thin film layer on the top surface, which will affect the absorption of the laser beam. For example, the absorptivity of solid Al varies, depending on surface roughness, between 0.1 and 0.4 for a wavelength of 1070 nm.<sup>29</sup> The role that such large variations in absorptivity play on molten pool size and temperature profiles was evaluated in Fig. 5, which shows the spatial and temporal evolution of the molten pool with initial absorptivity values of 0.1 (Fig. 5(a)) or 0.4 (Fig. 5(b)). At the melting point of silicon, an absorptivity corresponding to that of liquid Si, which is 0.223, is used. It can be observed that, after 1  $\mu$ s, the impact of having widely varying values for absorptivity on molten pool dimensions is significant. After 15  $\mu$ s though, the temperature profiles and molten pool dimensions become similar and are nearly identical at 30  $\mu$ s. Therefore, the large range in the reported values of absorptivity

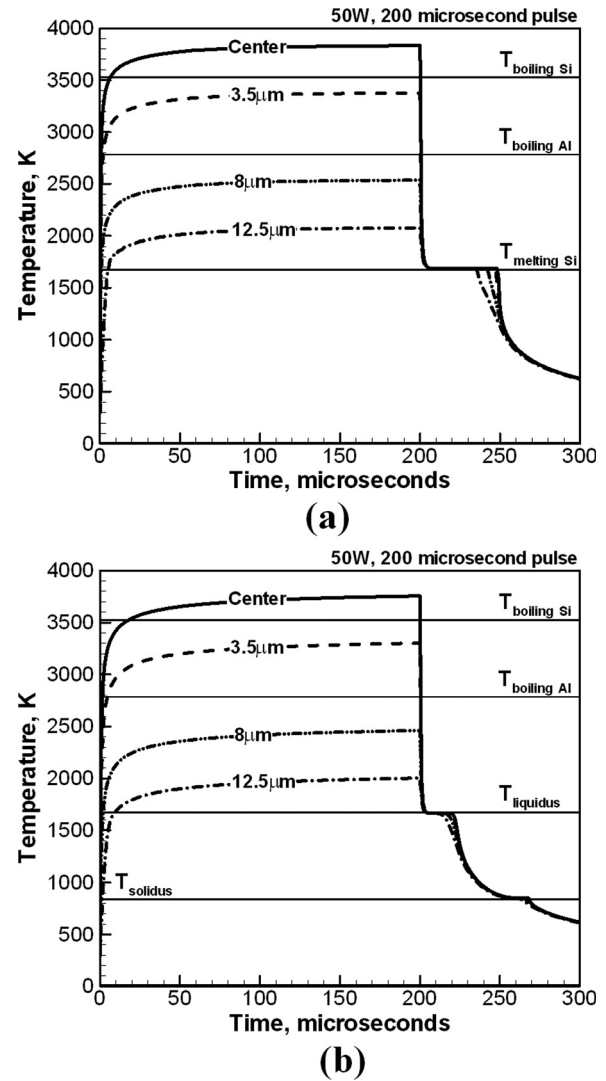


FIG. 8. Thermal cycles for (a) pure vs (b) Al-Si alloy with 50-W laser power and 200- $\mu$ s pulse duration exhibit different heating and cooling behavior due to the presence of Al in the melt. The distance values shown on different lines indicate the distance from the center of the molten pool.

for solid Al does not affect the computed temperature profiles and spot dimensions for pulse durations greater than 30 microseconds. Consequently, the absorptivity of liquid silicon is used for the millisecond level pulse durations considered here.

In order to examine the role that the aluminum thin film plays in determining the molten pool size, two simulations were performed. The first one involved the processing of a silicon wafer without the aluminum thin film, and the second one considered the aluminum thin film and the mixing of aluminum and silicon in the molten pool. A comparison between experimental spots and computed molten pools for the two cases is shown in Fig. 6(a) for the Si substrate and Fig. 6(b) for the silicon wafer coated with the aluminum thin film for a laser power of 18 W and a pulse duration of 19 ms. It is observed that the size of the computed molten pool is significantly over-predicted when assuming a pure Si substrate, whereas the calculated pool width agrees well with experimental results when considering an Al-Si alloy. The motion of the liquid Si in the molten pool is due to

Marangoni convection, which results from the spatial variation of surface tension along the surface of the pool. The surface tension of Si strongly decreases with an increase in temperature, which causes the fluid to flow from the center (high temperature region) to the periphery (low temperature region).

In Fig. 6(b), the alloy contains 24.6 wt. % Al, based on calculations using Eq. (10), which corresponds to a liquidus temperature of 1551 K using Eq. (9). When accounting for Al, the total enthalpy for the system immediately increases at the eutectic temperature, due to the instantaneous formation of liquid, as shown in Fig. 4. A larger fraction of the supplied energy is required to melt the material, and the temperature does not rise as rapidly as it would for pure Si and the molten pool does not grow as large for the alloy. Figure 7 shows that the concentration of Al changes with time during the first 0.2 ms and becomes constant thereafter for all three power levels. The concentration of Al in the molten pool is determined after every time step considering

the changes in the molten pool dimensions. As the pulse duration is increased, the molten pool dimensions experience little change after 200  $\mu$ s, and the Al concentration reaches a steady state at 24.6, 7.8, and 4.5 wt. % for laser powers of 18 W, 34 W, and 50 W, respectively.

Figures 8(a) and 8(b) show the thermal cycles for a pure material and an Al-Si alloy at 50 W laser power and a 200  $\mu$ s pulse, respectively. In Fig. 8(a), a long thermal arrest is observed on cooling at the melting point of Si due to the large difference in the enthalpy at the melting temperature between solid silicon (1286 kJ kg<sup>-1</sup>) and liquid silicon (3085 kJ kg<sup>-1</sup>). Despite the large latent heat of fusion for pure Si, the amount of energy supplied from the laser is sufficient to induce rapid phase change from solid to liquid on heating. The heating rate within the molten pool is on the order of 10<sup>9</sup> K sec<sup>-1</sup>, and the elevated temperatures within the pool are maintained for the entire 200- $\mu$ s pulse duration with minimal increase. The temperature varies from 3832 K at the center of the pool to 1687 K at the solid/liquid interface over a distance of approximately 22.8  $\mu$ m. Due to the large spatial variation of surface tension with temperature, the maximum velocities are approximately 5.2 m sec<sup>-1</sup>.

With such high velocities, substantial mixing within the molten pool is expected at this pulse duration. When comparing the thermal cycles in Fig. 8(a) and Fig. 8(b), it is evident that the temperatures in the molten region are lower for the binary alloy than that for pure Si over the entire course of the laser pulse. The peak temperatures within the molten pool are about 100 K higher for the pure material during the 200  $\mu$ s pulse. The cooling curves shown in Fig. 8(b) are substantially different from that for pure silicon. Specifically, there are two discernable thermal arrests for the alloy located at the liquidus and eutectic temperatures.

As the power level is varied and the concentration of Al in the molten pool changes, the observed cooling cycles change as well, since the liquid to solid transformations that take place at the liquidus and eutectic temperatures will be composition dependent. As the concentration of Al is increased, which will correspond to the use of lower power levels, a larger fraction of the transformation will take place at the eutectic temperature. However, as the concentration is decreased and the liquid alloy more closely resembles a pure material, a significant portion of the liquid to solid transformation will take place at the liquidus temperature. As a result, the substrate can spend a significant amount of time at elevated temperatures. In both cases (pure versus binary alloy), the cooling cycles are similar after the eutectic temperature is reached. The rate of cooling, however, is much greater for pure silicon than for the binary alloy, since the entire liquid to solid transformation takes place at the melting temperature (1687 K).

Figure 9 shows the calculated spot sizes for a binary Al-Si alloy at a power level of 50 W and pulse durations of 4 ms and 19 ms. The calculated molten pool widths agree well with the experimental results for both cases. Since the temperatures within the pool are above the boiling point of both Si (3514 K) and Al (2792 K) at the center, as shown in the temperature profiles for Fig. 8(b), it can be expected that substantial vaporization of alloying elements will take place.

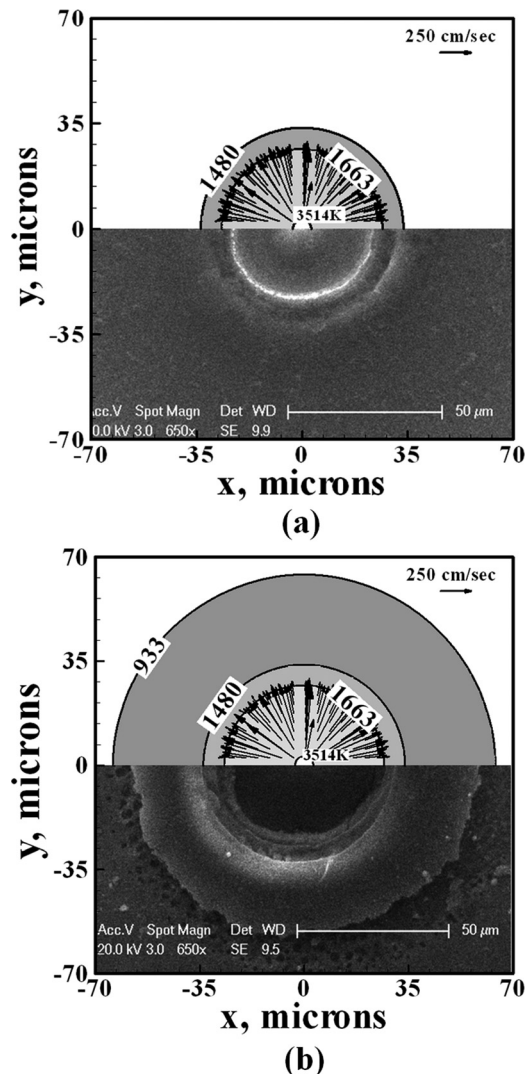


FIG. 9. Comparison of calculated and experimental (Ref. 13) molten pool sizes for Al-Si shows improved fit for molten zone for (a) 50 W, 4.6 wt. % Al, 4 ms pulse duration and (b) 50 W, 4.6 wt. % Al, 19 ms pulse duration. Contours identified on the plot are: Al melting temperature (933 K),  $\alpha$ -Si:H (1480 K), and liquidus temperatures (1663 K).

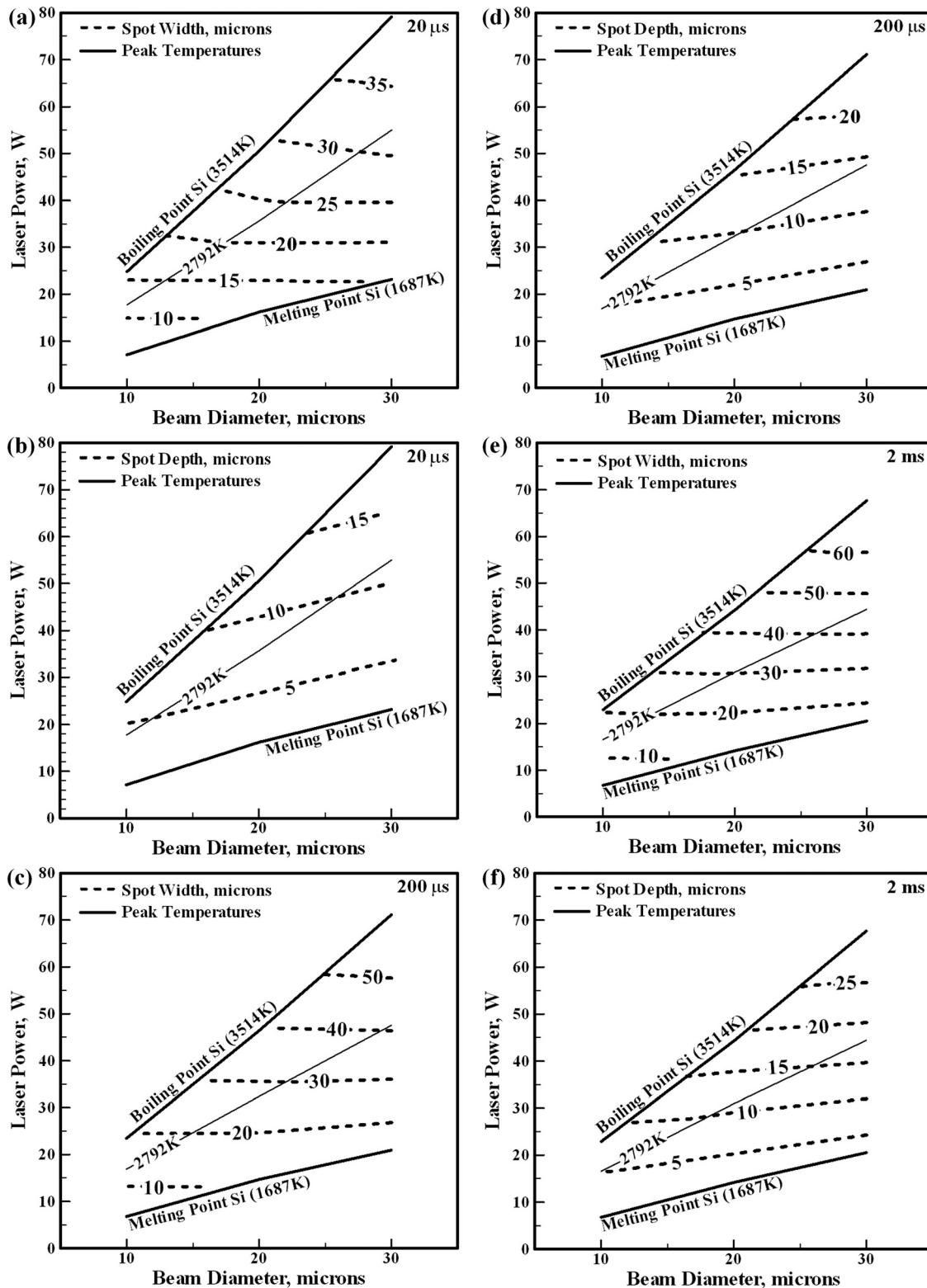


FIG. 10. Computed molten pool width and depth are shown as a function of laser power and beam diameter for assistance in selection of appropriate processing parameters at (a)–(b) 20  $\mu\text{s}$ , (c)–(d) 200  $\mu\text{s}$ , and (e)–(f) 2 ms.

This can be confirmed in Fig. 9(b), where noticeable substrate damage is observed as the pulse duration is increased from 4 ms to 19 ms. The alignment of important temperature contours for the molten region (1663 K) and the melting temperature of Al (933 K) shows fair agreement with the regions of delamination observed in the experimental results. Small differences between the computed molten pool sizes and

experimental results can be attributed to errors in the estimation of the actual amount of dissolved Al. Here, the estimated concentration of Al assumes that the Al content present in the molten pool comes solely from the melting of the thin-film layer directly above the molten region. However, the actual amount of Al in the molten region may be slightly higher than the computed values, since the thin film

covers the entire substrate and the surface temperatures away from the molten region will also be above the melting temperature of Al.

Based on the agreement between the calculated and experimental results over a wide range of pulse durations and power levels, process maps have been developed to identify safe operating regimes. Figures 10(a) through 10(f) show process maps for the contact width and contact depth as a function of power levels up to 80 W and laser beam diameters between 10  $\mu\text{m}$  and 30  $\mu\text{m}$  for pulse durations of 20  $\mu\text{s}$ , 200  $\mu\text{s}$ , and 2 ms. These pulse durations were selected because noticeable differences in the processing windows are observed over this range. Since alloy formation between the Si and Al is critical to achieve the ohmic contact, the peak temperature should remain between the melting and boiling points for the material under consideration. Since the alloy content can vary with power level, the melting temperature of Si (1687 K), the boiling temperature of Al (2792 K), and the boiling temperature of Si (3514 K) have been used to define safe operating windows for the process. The upper limits have been selected to avoid significant metal loss through vaporization of Al and Si and ejection of particulates. The computed results in Fig. 10 show that the practical range of appropriate laser powers becomes rather narrow when a smaller beam radius is selected for all pulse durations. This behavior is consistent with the fact that an increase in the power density will lead to a rapid rise in the peak temperature above the boiling point of both Al and Si.

At 20- $\mu\text{s}$  pulse durations, the process window is substantially larger for larger beam diameters, since the peak temperatures do not exceed the boiling point of Al and Si within this time frame. As the pulse duration is increased, however, the processing window shrinks as the process trends toward minimal increase in peak temperature and spot growth. At 20  $\mu\text{s}$ , however, the spot size is considerably smaller for the same processing parameters. For instance, the spot width is only 30  $\mu\text{m}$  when using a power of 50 W and beam diameter of 30  $\mu\text{m}$ . For the same parameters, the spot width grows to 40  $\mu\text{m}$  at 200  $\mu\text{s}$  and 50  $\mu\text{m}$  at 2 ms. In addition, the contact width and depth remain fairly constant with changes in beam diameter at the same power level. For instance, at 40 W laser power, one can achieve similar contact geometry for a 200- $\mu\text{s}$  pulse with both a 20- $\mu\text{m}$  beam diameter and a 30- $\mu\text{m}$  beam diameter. By utilizing a 30- $\mu\text{m}$  beam diameter, however, one can ensure that the processing temperatures do not exceed the boiling point of Al and thereby eliminate the possible loss of important alloying elements. The computed results in Fig. 10 provide guidance as to how the depth and width of the weld pool can vary during laser processing as a function of beam radius and laser power. An important feature of the results in Fig. 10 is that a particular contact size can be achieved through multiple combinations of processing parameters. Such flexibility can be worthwhile in determining what parameters to use to obtain a specific contact size while minimizing high temperature exposure to substrate.

As has been shown above, a particular molten pool size can be obtained from various combinations of laser processing variables. However, the computed peak temperatures and

thermal cycles may vary, resulting in one processing condition being more desirable than others. Figure 11 shows the changes in the computed temperatures along the top surface within the molten region for two conditions that produce the same geometry (20- $\mu\text{m}$  and 30- $\mu\text{m}$  laser beam diameters for 40-W laser power and 200- $\mu\text{s}$  pulse duration). In these two cases, the diameters of the molten pool are the same (30  $\mu\text{m}$ ). With a laser beam diameter of 20  $\mu\text{m}$ , the computed peak temperature reaches 3225 K, while that for a 30- $\mu\text{m}$  beam diameter reaches only 2546 K. Since the pool width is approximately the same for both beam diameters, the temperature gradient using a smaller beam diameter is much greater. As a result, the fluid flow velocities calculated are approximately two times larger for the smaller beam diameter. Although these elevated temperatures can lead to greater mixing of the molten region, they can also lead to a significant loss of alloying elements.

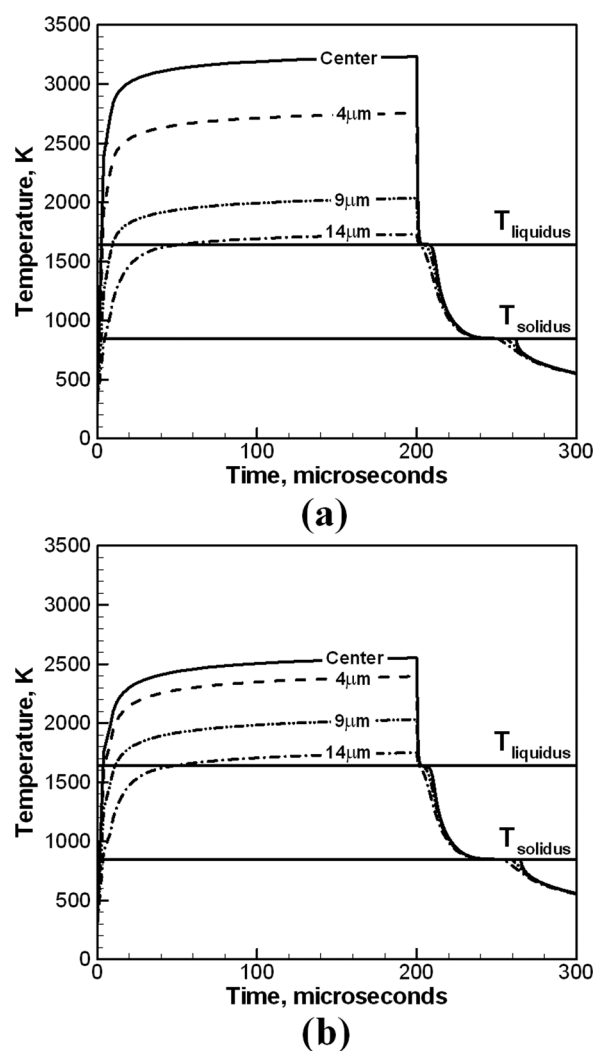


FIG. 11. Thermal cycles for top surface of molten pool with 40-W laser power and 200- $\mu\text{s}$  pulse duration for (a) 20- $\mu\text{m}$  beam diameter and (b) 30- $\mu\text{m}$  beam diameter. The distance values shown on different lines indicate the distance from the center of the molten pool.



## SUMMARY AND CONCLUSIONS

The evolution of molten pool geometry and temperature and velocity fields was calculated for a Si substrate coated with an Al thin film using a three-dimensional transient numerical heat transfer and fluid flow model. By accounting for the presence of Al in the molten pool, the accuracy of the computed molten pool widths was significantly improved and agreed well with experimental results. The variables studied include laser powers between 18 to 50 W, pulse durations of 4 ms to 19 ms, and an Al thin film thickness of 0.5  $\mu\text{m}$ .

The addition of Al to the molten region significantly alters the thermal cycles. As the amount of Al is increased, the temperatures within the molten region can decrease substantially for the compositions considered. For pure Si, a thermal arrest is observed during the transformation of liquid to solid due to the evolution of the latent heat of fusion. The cooling cycles are drastically different when Al is present, since the liquid-to-solid transformation occurs over a very large two-phase region.

The computed temperature gradients within the molten pool can be substantially different, depending on the laser beam diameter. Furthermore, use of a large beam diameter can allow for obtaining similar contact size when the processing time is carefully chosen while substantially reducing the temperature gradients within the pool, which can affect the solidification process.

Numerically computed process maps demonstrate that the safe operating regime for selection of laser power is restricted as spot size is reduced. As the pulse duration is increased from tens of microseconds to hundreds of microseconds, the operating window shrinks to avoid peak temperatures exceeding the boiling point of Si. The process maps demonstrate that multiple combinations of laser power, spot size, and pulse duration exist to obtain a given contact size.

## ACKNOWLEDGMENTS

The work was supported by a grant from the American Welding Society as well as BP Solar. Experimental work was performed at the Applied Research Laboratory at Penn State University, whose work is supported by a grant from BP Solar. The authors thank Dr. Ted Reutzel, Dr. Suzanne Mohny, Dr. Lian Zou, and Dr. Dave Carlson for their interest in this work. The authors also thank Dr. Rohit Rai for assistance with development of the binary alloy modeling methodology.

- <sup>1</sup>J. Mueller, K. Bothe, S. Gatz, F. Haase, C. Mader, and R. Brendel, *J. Appl. Phys.* **108**, 124513 (2010).
- <sup>2</sup>A. Wolf, D. Biro, J. Nekarda, S. Stumpp, A. Kimmerle, S. Mack, and R. Preu, *J. Appl. Phys.* **108**, 124510 (2010).
- <sup>3</sup>E. Schneiderlochner, R. Preu, R. Ludemann, and S. W. Glunz, *Prog. Photovoltaics* **10**, 29 (2002).
- <sup>4</sup>E. Schneiderlochner, A. Grohe, C. Ballif, S. W. Glunz, R. Preu, and G. Willeke, Photovoltaic Specialists Conference, Conference Record of the Twenty-Ninth IEEE, 0-7803-7471-1, 300 (2002).
- <sup>5</sup>W. Brendle, V. X. Nguyen, A. Grohe, E. Schneiderlochner, U. Rau, G. Palfinger, and J. H. Werner, *Prog. Photovoltaics* **14**, 653 (2006).
- <sup>6</sup>M. Tucci, E. Talgorn, L. Serenelli, E. Salza, M. Izzi, and P. Mangiapane, *Thin Solid Films* **516**, 6767 (2008).
- <sup>7</sup>U. Zastrow, L. Houben, D. Meertens, A. Grohe, T. Brammer, and E. Schneiderlochner, *Appl. Surf. Sci.* **252**, 7082 (2006).
- <sup>8</sup>E. Van Kerschaver and G. Beaucarne, *Prog. Photovoltaics* **14**, 107 (2006).
- <sup>9</sup>X. He, P. W. Fuerschbach, and T. DebRoy, *J. Phys. D* **36**, 1388 (2003).
- <sup>10</sup>M. M. Collur and T. DebRoy, *Metall. Trans. B* **20**(2), 277 (1989).
- <sup>11</sup>X. He, T. DebRoy, and P. W. Fuerschbach, *J. Appl. Phys.* **94**, 6949 (2003).
- <sup>12</sup>X. He, P. W. Fuerschbach, and T. DebRoy, *J. Appl. Phys.* **96**, 4547 (2004).
- <sup>13</sup>B. Hedrick, B. DeCesar, B. P. Downey, S. E. Mohny, J. Flemish, L. Zou, and E. W. Reutzel, "Processing conditions and characterization of laser-fired contacts for solar cell devices" (unpublished).
- <sup>14</sup>Internal communication, BP Solar, 2011.
- <sup>15</sup>O. W. Dillon, Jr. and C. T. Tsai, *J. Cryst. Growth* **82**, 50 (1987).
- <sup>16</sup>N. H. Nickel, *Laser Crystallization of Silicon* (Elsevier, London, 2003).
- <sup>17</sup>B. Fischer, Ph.D. dissertation, University of Konstanz, 2003.
- <sup>18</sup>X. He, J. T. Norris, P. W. Fuerschbach, and T. DebRoy, *J. Appl. Phys.* **39**, 525 (2006).
- <sup>19</sup>X. He, J. W. Elmer, and T. DebRoy, *J. Appl. Phys.* **97**, 084909 (2005).
- <sup>20</sup>A. Paul and T. DebRoy, *Metall. Trans. B* **19**, 851 (1988).
- <sup>21</sup>P. A. A. Khan and T. DebRoy, *Metall. Trans. B* **15**, 641 (1984).
- <sup>22</sup>M. M. Collur, A. Paul, and T. DebRoy, *Metall. Trans. B* **18**, 733 (1987).
- <sup>23</sup>K. Mundra and T. DebRoy, *Metall. Trans. B* **24**, 145 (1993).
- <sup>24</sup>W. Zhang, C. H. Kim, and T. DebRoy, *J. Appl. Phys.* **95**(9), 5220 (2004).
- <sup>25</sup>H. Zhao and T. DebRoy, *Metall. Trans. B* **32**, 163 (2001).
- <sup>26</sup>S. V. Patankar, *Numerical Heat Transfer and Fluid Flow* (Hemisphere, New York, 1980).
- <sup>27</sup>*Smithells Metals Reference Book*, 7th ed., edited by E. A. Brandes and G. B. Brook (Butterworth Heinemann, Oxford, 1992).
- <sup>28</sup>J. F. Ready and D. F. Farson, *LIA Handbook of Laser Materials Processing* (Magnolia, Orlando, 2001).
- <sup>29</sup>G. E. Jellison, *Semiconductors and Semimetals* **23**, 95–164 (1984).
- <sup>30</sup>W. K. Rhim and K. Ohsaka, *J. Cryst. Growth* **208**, 313 (2000).
- <sup>31</sup>A. De and T. DebRoy, *Sci. Technol. Weld. Joining* **11**(2), 143 (2006).
- <sup>32</sup>A. De and T. DebRoy, *J. Appl. Phys.* **95**(9), 5230 (2004).
- <sup>33</sup>J. L. Murray and A. J. McCalister, *Bull. Alloy Phase Diagrams* **5**(1), 74 (1984).
- <sup>34</sup>L. B. Pakratz, *Thermodynamic Properties of Elements and Oxides* (U.S. Dept. of Interior, Bureau of Mines, Washington, 1982).
- <sup>35</sup>C. J. Glassbrenner and G. A. Slack, *Phys. Rev.* **134**(4A), A1058 (1964).
- <sup>36</sup>E. Yamasue, M. Susa, H. Fukuyama and K. Nagata, *J. Cryst. Growth* **234**, 121 (2002).
- <sup>37</sup>D. F. Gibbons, *Phys. Rev.* **112**(1), 136 (1958).
- <sup>38</sup>A. M. Korolkov, *Casting Properties of Metals and Alloys*, (Consultants Bureau, New York, 1963), p. 37.